

Computational investigation of Spherical Aberration with Geometrical Optics

Xuheng Zhao

Abstract—With diffraction ignored in geometrical optics, spherical aberration was investigated by simulating a series of optical elements with Python. The single spherical surface, the plano-convex lens in both orientations, and the biconvex lens with optimised curvatures were successively modelled, and the related ray trajectories were plotted. By calculating the RMS spot radii for all the cases and optimising the orientations and curvatures for the lens, the spherical aberration was decreased by a total of 82% for a singlet lens system. For the biconvex lens that experienced the smallest aberrations, the diffraction limit was exceeded under the given aperture radius, and thus suggested that the best performance of a singlet lens was reached under the limit of geometrical optics.

I. INTRODUCTION AND THEORY

IN the limit of geometrical optics where diffractions are ignored, light propagations are formulated with rays perpendicular to the wavefronts of the light. Since the wave speed changes when it travels from one medium to another, the wave direction is changed according to Snell's law of

$$n_i \sin \theta_i = n_f \sin \theta_f, \quad (1)$$

where n_i and n_f are the refractive indices of the initial and the final mediums that the wave propagates through, and θ_i and θ_f are the incident and the refractive angles respectively.

The vector form of (1) is given as

$$\widehat{k}_f = \left(\frac{n_i}{n_f} \right) \widehat{k}_i + \left(\cos \theta_f - \frac{n_i}{n_f} \cos \theta_i \right) \widehat{n} \quad (2)$$

where \widehat{k}_i and \widehat{k}_f are the normalised vector for the incident and the refracted ray directions accordingly, and \widehat{n} is the normalised vector of the interface plane, which points from the interface to the final medium, or n_f [1].

When applying (1) and (2) to a uniform collimated beam incident onto a spherical surface, if n_i is smaller than n_f , the non-paraxial rays would focus before the paraxial ones do, and thus a blurry image is produced at the paraxial focus [1], [2]. This phenomenon is called the spherical aberration, and the aberration scale can be measured via calculating the root mean square (RMS) spot radius of the ray positions at the paraxial focus [3].

For a simple optical system consisting only one singlet lens and monochromatic light, the limit of obtaining significant diffractions, d , is governed by

$$d = \frac{\lambda f_p}{2R_a} \quad (3)$$

where λ is the wavelength of the light, f_p is the paraxial focal length of the lens, and R_a is the aperture radius [2], [3].

II. METHODS

A. Preliminary tests using a single spherical surface

The simulation was constructed in a three-dimensional (3D)

Cartesian coordinate, and (2) was implemented. Since the spherical surfaces were able to form images, a simple performance test was conducted with a small surface as shown in Fig 1, where the curvature, $\frac{1}{R_1}$, of the surface was 1 mm^{-1} , and the refractive indices were $n_i = 1$ and $n_f = 1.5$. Regarding the two intercepts at $z = -5$ as the top and bottom of a light-emitting object, the two intercepts at $z \approx 4$ would be the image formed after passing through the surface. The object was located beyond twice the focal lengths, and the image was formed between one and two focal lengths as expected. Moreover, the image was vertically inverted comparing to the object, which further suggested that the performance of the spherical surface was well simulated.

To investigate the ray-focusing performance of a spherical surface, a few non-paraxial rays were traced through a larger spherical surface with $\frac{1}{R_1} = 0.03 \text{ mm}^{-1}$, $n_i = 1$, and $n_f = 1.5$ as shown in Fig. 2. The value of f_p was estimated via propagating a paraxial ray with 1 mm distant from the optical axis and measuring its focal length [3], which gave the coordinate of the paraxial focus at $z = 200$. Comparing to the focal point formed by the non-paraxial rays at $z \approx 175$, the focal length was shortened by 25%. Thus, the presence of spherical aberrations could be confirmed.

B. Modelling a single spherical surface

For further investigation of the spherical aberrations for a single spherical surface, a uniform collimated beam, or a ray bundle, was generated around the optical axis. The rays were evenly spread with uniformly increasing number, such as 6, 12, 18, etc., onto successive concentric circles with uniformly increasing radii, such as 1 mm, 2 mm, 3 mm, etc., as shown in Fig. 3. The radius of the ray bundle, r_{bun} , shown in Fig. 3 was set to 5 mm, and it was then propagated through a surface of $\frac{1}{R_1} = 0.03 \text{ mm}^{-1}$ with $n_i = 1$ and $n_f = 1.5168$ for simulating air and glass respectively. The ray trajectories in 3D and 2D were presented in Fig. 4 a) and b) correspondingly. By estimating f_p with the same technique as that in Section II A, an output plane was positioned at the paraxial focus to obtain the ray positions shown in Fig. 5.

C. Modelling a plano-convex singlet lens

To improve the performance of the single spherical surface, a plano-convex lens was simulated by positioning a plano surface at the distance of 5 mm from a spherical surface. The curvature of the spherical surface was 0.02 mm^{-1} and the refractive index that surrounded the lens, n_{sur} , was 1 and that inside the lens, n_{in} , was 1.5168. The same ray bundle with $r_{bun} = 5 \text{ mm}$ was propagated through the plano-convex and the convex-plano orientations separately as shown in Fig. 6 a) and b) accordingly. The f_p value was determined again using

the technique in Section II A, and an output plane was positioned at the paraxial focus to terminate the rays.

Since the f_p values were different between the two orientations, a series of ray bundles with increasing radii were propagated individually through each orientation. The RMS spot radii were plotted against the ray bundle radii for both orientations as shown in Fig. 7.

D. Optimisation for a singlet biconvex lens

As shown in Fig. 7, although the convex-plano orientation experienced less spherical aberrations than the plano-convex one, the performance of a singlet lens could be further improved by implementing a biconvex lens with two surface curvatures optimised to give the least aberrations [3]. The initial guesses of the optimisation were $\frac{1}{R_1} = 0.02 \text{ mm}^{-1}$ and $\frac{1}{R_2} = -0.0015 \text{ mm}^{-1}$ for the first and second curvatures respectively. Other parameters were chosen to be the same as that of the convex-plano lens in Section II C, where $f_p = 98.453 \text{ mm}$, $n_{sur} = 1$, $n_{in} = 1.5168$, and the distance between the two surfaces was 5 mm. The same ray bundle with $r_{bun} = 5 \text{ mm}$ was propagated through the lens, and the $\frac{1}{R_1}$ and $\frac{1}{R_2}$ values were varied using *scipy.optimize.fmin* until the smallest RMS spot radius was obtained at the paraxial focus. The ray trajectories for the optimised biconvex lens were plotted as shown in Fig. 8.

III. RESULTS AND DISCUSSIONS

A. Data analysis and results

The parameters of each optical element and their related aberration scales, or the RMS spot radius, were displayed in Table I. The diffraction limits with $R_a = r_{bun} = 5 \text{ mm}$ were also calculated according to (3), where λ was set to 588 nm.

TABLE I
SPHERICAL ABERRATION SCALE AND DIFFRACTION LIMIT FOR THE
OPTICAL ELEMENTS

| Optical element | $\frac{1}{R_1}$ (mm^{-1}) | $\frac{1}{R_2}$ (mm^{-1}) | f_p (mm) | RMS spot radius (mm) | Diffraction limit (mm) |
|-----------------|---|---|---------------|----------------------------|------------------------------|
| Single | 0.03 | - | 97.833 | 0.01582 | 0.00575 |
| Plano-convex | 0 | -0.02 | 101.749 | 0.03723 | 0.00598 |
| Convex-plano | 0.02 | 0 | 98.453 | 0.00934 | 0.00579 |
| Biconvex | 0.0185 | -0.0016 | 98.453 | 0.00281 | 0.00579 |

The RMS spot radius for a plano-convex lens was more than twice of that of the single spherical surface, but the RMS spot radius for the convex-plano lens was 41% lower than that of the single spherical surface. Moreover, with the convex-plano lens replaced by the optimised biconvex lens, the RMS spot radius was further decreased by 70%, giving a total decrement of 82% when comparing the biconvex lens with the single spherical surface.

For the plano-convex lens performance as shown in Fig. 7, the plano-convex lens always experienced more spherical aberrations than the convex-plano lens. This obeyed (1) as the rays were not bent at first surface of the plano-convex lens but were bent more significantly at the second surface due to the decrease in the refractive index.

For the optimised biconvex lens, since the diffraction limit was twice as large as the RMS spot radius, the main trigger

of forming a blurry image would be from the diffractions rather than the spherical aberrations. This was further supported by Fig. 9, where the RMS spot radii were compared with the diffraction limits, which the value of diffraction scale became larger than that of the RMS spot radius when r_{bun} , or R_a , was decreased to around 5 mm. However, for all the other optical elements, the diffraction limits were less than the RMS spot radii, suggesting these systems were not diffraction limited. Therefore, under the limit of geometrical optics where diffractions were ignored, the best performance of a singlet lens was reached with the optimised biconvex lens with $R_a = 5 \text{ mm}$.

B. Discussions

When switching from the single spherical surface to the convex-plano and then the biconvex lens, the decrease in the spherical aberrations was expected as rays would be diverged when crossing the second surface of the lens according to (1). Moreover, the ratio of $\frac{R_2}{R_1}$ for the biconvex lens was about -12, which suggested that the spherical aberration would be mostly minimised for an optical system involving air and a glass-made singlet [2]. Hence, the argument that the performance of a singlet lens was maximised with the optimised biconvex lens would be reasonable.

However, in practice, keeping R_a as small as 5 mm would reduce the light intensity of the image formed, and thus limited the functionality of the optical system [1]. On the other hand, increasing R_a would induce even more severe aberrations for the non-paraxial rays. Yet, with the R_a values increased and λ kept at constant, the diffraction effect would be reduced according to (3), and by using a combination of a converging and a diverging lens, the spherical aberration could be minimised [1]. Thus, to improve the performance of the optical system used in this investigation, more investigations could be carried out with a non-singlet lens and with larger values of R_a .

IV. CONCLUSIONS

The spherical aberration with monochromatic light propagated through a converging singlet was simulated successfully. By implementing the optical elements of a single spherical surface, a plano-convex lens in both orientations, and finally an optimised biconvex lens, the RMS spot radius, or the aberration scale, was decreased to 0.00281 mm, which was 82% less than that of the single spherical surface. With $R_a = 5 \text{ mm}$, diffraction limit of the biconvex lens was about twice as much as the RMS spot radius, suggesting the diffraction limit was exceeded for the system.

Improvements such as increasing R_a and using a non-singlet lens can be implemented [1].

V. REFERENCES

- [1] E. Hecht, Optics. Pearson Education India, 2012.
- [2] A. Lipson, S. G. Lipson and H. Lipson, Optical Physics. Cambridge University Press, 2010.
- [3] D. Colling and C. Paterson, "Project A: An Optical Ray Tracer," unpublished.

VI. LIST OF PLOTS

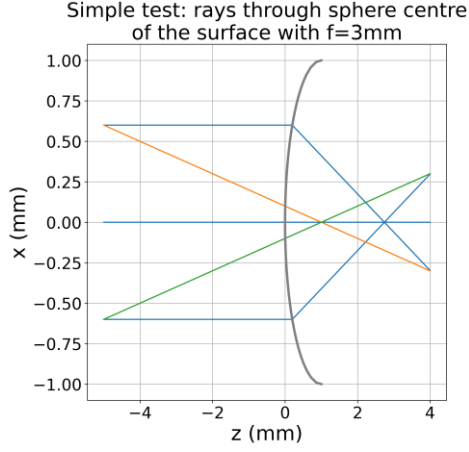


Fig. 1. A simple performance test involving a single spherical surface with $\frac{1}{R_1} = 1 \text{ mm}^{-1}$, $n_i = 1$, and $n_f = 1.5$. The rays were originated at $|x| = 0.6$ and $z = -5$, and two rays parallel to the optical axis and two rays crossing through the sphere centre were traced. They formed two intercepts at $z \approx 4$, which was expected according to the imaging properties of a converging optical element.

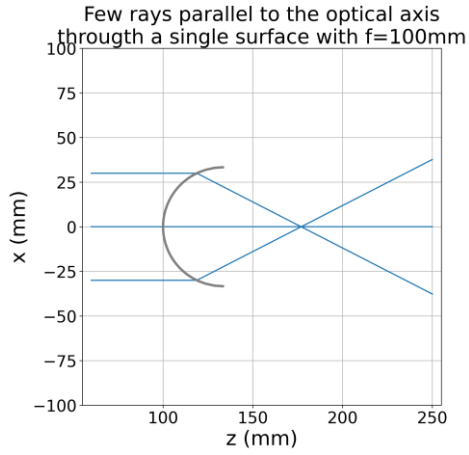


Fig. 2. Tracing three non-paraxial rays through a single spherical surface with $\frac{1}{R_1} = 0.03 \text{ mm}^{-1}$, $n_i = 1$, and $n_f = 1.5$. The coordinate of the paraxial focus was calculated as $z = 200$, and the coordinate of the focal point formed by the non-paraxial rays was at $z \approx 175$. The focal length was shortened by 25% between the paraxial and non-paraxial rays.

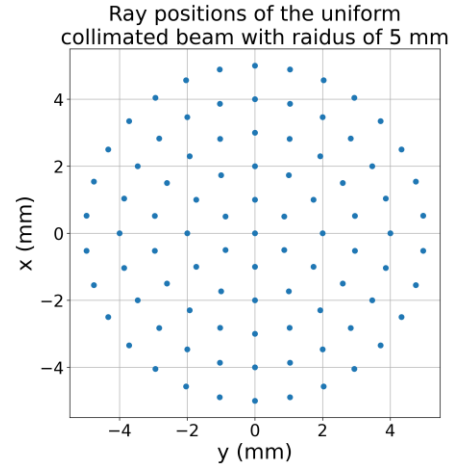
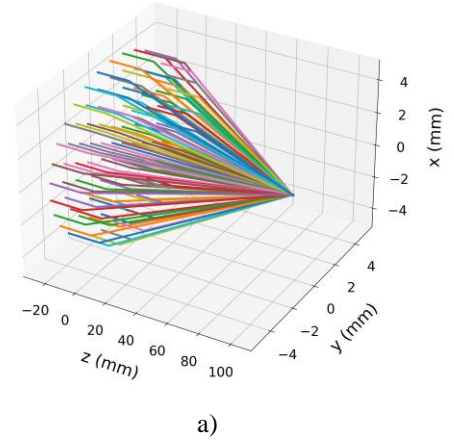


Fig. 3. The uniform collimated beam, or the ray bundle, generated with $r_{bun} = 5 \text{ mm}$. For successive concentric circles, the number of rays was increased by six, and the circle radii was increased by 1 mm.

3D plot for a non-paraxial uniform ray bundle through a single surface with $f=97.833\text{mm}$



2D plot for a non-paraxial uniform ray bundle through a single surface with $f=97.833\text{mm}$

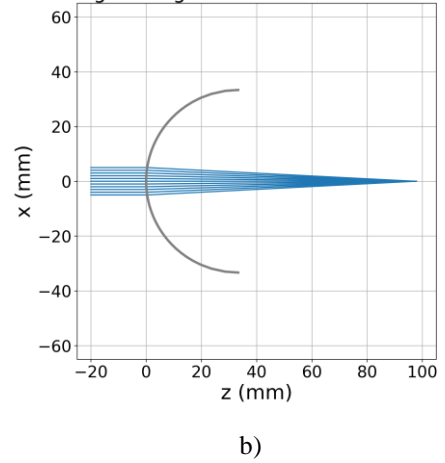


Fig. 4. The ray trajectories in a) 3D and b) 2D for a single spherical surface with $\frac{1}{R_1} = 0.03 \text{ mm}^{-1}$, $n_i = 1$, and $n_f = 1.5168$. The ray bundle with $r_{bun} = 5 \text{ mm}$ was propagated through the surface and then terminated at the paraxial focus with coordinate of $z = 97.8$.

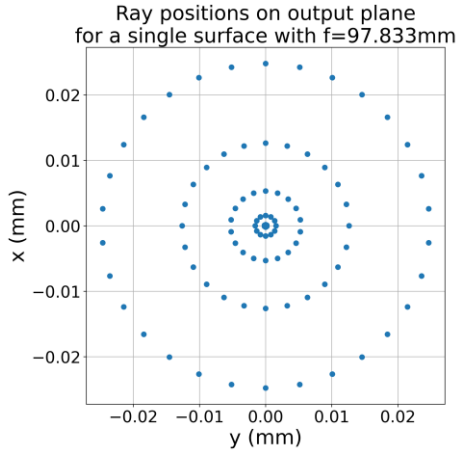
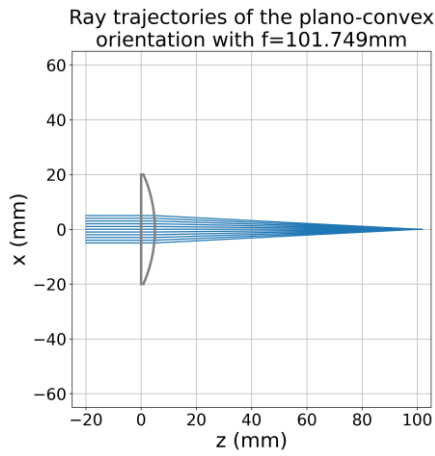
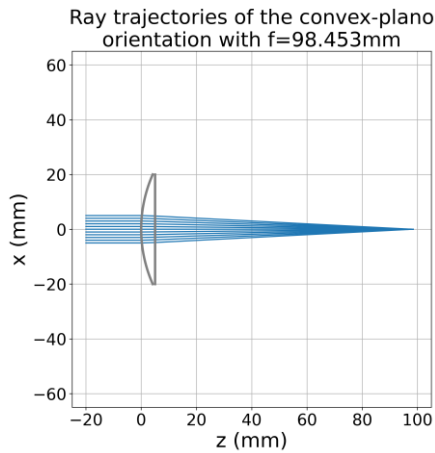


Fig. 5. The ray positions on the output plane at $z = 97.8$ for the system shown in Fig 4.



a)



b)

Fig. 6. The ray trajectories for a) the plano-convex and b) the convex-plano lens orientations with $n_{sur} = 1$ and $n_{in} = 1.5168$. The curvature of the spherical surface was 0.02 mm^{-1} . The same ray bundle with $r_{bun} = 5 \text{ mm}$ was propagated through both orientations separately and then terminated at the paraxial focus for each. The f_p value of the plano-convex was slightly longer than that of the convex-plano.

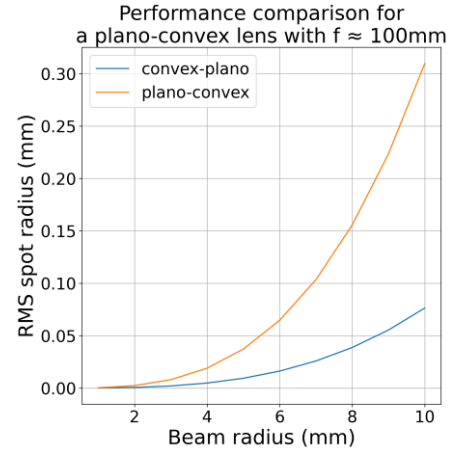


Fig. 7. Performance, or the scale of the spherical aberrations, comparison between two orientations of the plano-convex lens shown in Fig. 6. The convex-plano orientation experienced less aberrations than the plano-convex one.

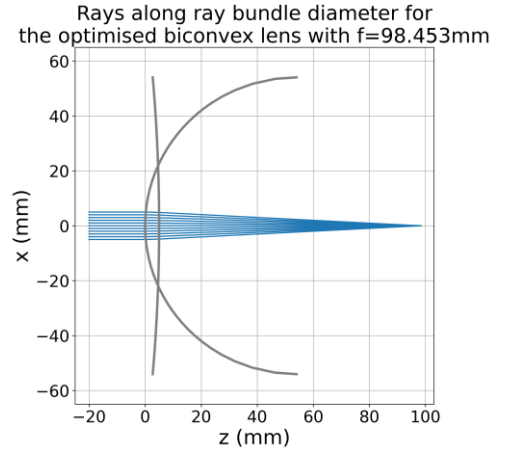


Fig. 8. The ray trajectories for the optimised biconvex lens with $n_{sur} = 1$ and $n_{in} = 1.5168$. The optimised curvatures were $\frac{1}{R_1} = 0.01850 \text{ mm}^{-1}$ and $\frac{1}{R_2} = -0.00156 \text{ mm}^{-1}$. The ray bundle with $r_{bun} = 5 \text{ mm}$ was propagated through the lens and then terminated at the paraxial focus with coordinate of $z = 98.5$.

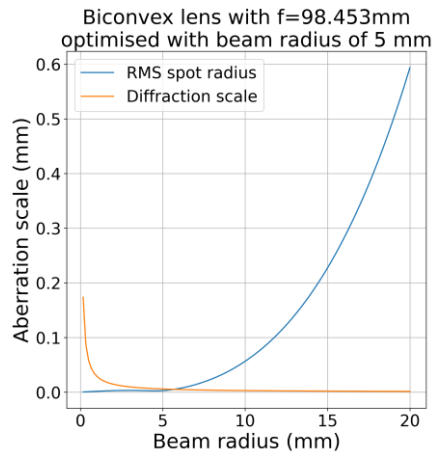


Fig. 9. Comparison between the RMS spot radii and diffraction limits for the optimised biconvex lens shown in Fig. 8. The beam radius, r_{bun} , was equal to R_a in (3). When r_{bun} , or R_a , decreased to around 5 mm, the system became diffraction limited as the value of diffraction scale was larger than that of the RMS spot radius.